



# Quantification of metallic coating failure on carbon fiber reinforced plastics using acoustic emission

Markus G.R. Sause\*, Ferdinand Haider, Siegfried Horn

University of Augsburg, Institute of Physics, D-86135 Augsburg, Germany

## ARTICLE INFO

### Article history:

Received 14 May 2009

Accepted in revised form 20 July 2009

Available online 30 July 2009

### Keywords:

Acoustic emission

Coating

Fracture mechanics

Pattern recognition

Carbon

Composites

## ABSTRACT

Carbon fiber reinforced plastic substrates were subsequently coated with an electrochemically applied nickel and an electroplated copper layer. The coating-substrate system was loaded in four-point bending and the acoustic emission from coating failure was recorded during loading. The acoustic emission signals were analyzed using pattern recognition and frequency analysis techniques. This approach yields three distinguishable types of acoustic emission signals, which are correlated to three different failure mechanisms: i) nickel cracking ii) copper cracking and iii) delamination between the two coating layers. To confirm the correlation between the types of acoustic emission signals and the respective failure mechanisms and to assess the validity of the acoustic emission method to describe mechanical failure, the micro-mechanical fracture energies released during mechanical loading were calculated based on microscopic measurements of the crack progress utilizing scanning electron microscopy and scanning acoustic microscopy. These energies were compared to the associated acoustic emission signals energy for each failure mechanism. We found the calculated micro-mechanical energy values to be proportional to the measured accumulated acoustic emission energy of the associated acoustic emission signal type. We conclude that the reported failure classification method offers the possibility to compare fracture toughness values in multilayered coatings with multiple failure types, derived solely from acoustic emission energies.

© 2009 Elsevier B.V. All rights reserved.

## 1. Introduction

During the last decades the usage of carbon fiber reinforced plastic structures (CFRP) in engineering applications has increased dramatically due to their uniquely high strength per weight ratio. Unfortunately, these lightweight structures often lack typically metallic properties like wear resistance, high electrical conductivity or gas impermeability. A metal coating can improve the properties of CFRP structures in this respect. For example, the typical permeation value of a pure CFRP structure can be reduced by one to two orders of magnitude by the application of a metallic coating [1]. In order to build a lightweight tank-system for liquid hydrogen storage several combinations of electroplated coatings, so called liners, were investigated within the scope of the European Union founded research-project StorHy [2]. In such applications, the suitability of the functional coatings depends sensitively on its mechanical properties, e.g. adhesion or fracture toughness. To determine the mechanical properties of such coatings several methods are commonly used. The adhesive strength between electroplated coatings and substrate is usually determined via peel-tests or pull-off tests. The fracture toughness of the coating can be determined using uniaxial tensile tests. The obtained values are used to compare the fracture

toughness of coatings relative to each other. All these methods do not take into account residual stress present after coating application, which can decrease the load limit of the coating-substrate system dramatically [3]. Hence, these methods allow a comparison between different coating-substrate compositions, but are not suitable to predict the real load limit of a metallic liner inside a pressurized tank vessel. Failures like microscopic cracks and delamination between coating and substrate can lead to a dramatic increase in the gas permeation value, which defines the real load limit of the thin metallic coatings in this case [1]. In the past acoustic emission (AE) has been applied for health monitoring of pressurized CFRP-vessels focusing on CFRP failure [4,5]. In addition several authors investigated damage accumulation in plasma sprayed coatings on metallic substrates using AE [6–8]. In our investigation we will instead focus on AE arising from nickel-copper coatings on CFRP, which indicate a failure of the coating, while the substrates mechanical integrity is still maintained.

To approximate the real stress-strain conditions on the outside of a pressurized vessel investigated in [2], four-point-bending experimental setup was chosen and applied to coated planar samples. Earlier, in-situ electron microscopy has been applied to accurately determine the failure initiation of coatings [9]. Here we describe the detection of failure initiation by acoustic emission analysis. Stress waves released from microscopic structural changes, which typically originate from crack progress, were detected as a function of the applied strain and attributed to different failure mechanisms. In

\* Corresponding author.

E-mail address: [markus.sause@physik.uni-augsburg.de](mailto:markus.sause@physik.uni-augsburg.de) (M.G.R. Sause).

particular, we find a correlation between the accumulated acoustic emission energy and the calculated fracture energies derived from microscopic observations and linear elastic fracture mechanics (LEFM) calculations.

## 2. Methodical background

### 2.1. Pattern recognition techniques

Various theoretical approaches state, that a correlation between acoustic emission signal parameters and crack orientation and crack mode exists [10,11]. This offers the possibility to distinguish the origin of the recorded waveforms based on differences in signal parameters using pattern recognition techniques. The original waveforms shape and frequency composition are altered by propagation of the wave in a dispersive medium. This originates from geometric spreading and velocity dispersion. In particular in the case of thin CFRP structures, sound waves propagate as different plate wave modes. This results in frequency dependent attenuation due to the different wave modes velocities [12]. Consequently, the crack orientation can only be successfully determined within a limited distance from the location of the AE-source based on the frequency composition of the AE-signal [5].

One of the major problems of pattern recognition techniques is an adequate evaluation of the classification results from different clustering approaches. To quantify the quality of a dataset partitioning, several methods are used. Most frequently, the first step in acoustic emission pattern recognition is an appropriate waveform parameter (feature) extraction. These features decrease the data complexity and are further used to describe the waveform. In a second step these features are normalized and projected to their principal components axis and are analyzed by clustering algorithms. The result is a classification of all waveforms of a dataset according to their similarity within the chosen parameter space.

Measures like Rand statistics and Wilks  $\lambda$ -value are used to describe the quality of such partitions, but are only suitable to compare the efficiency of different algorithms applied to the same feature selection, cluster number and projection method. In order to determine the appropriate number of separable types of acoustic emission signals another numerical evaluation of clustering results was established [13,14] based on investigations from Davies and Bow [15,16]. They used two numerical criteria  $R$  and  $\tau$  which can be calculated for any partition of a dataset independent of its number of clusters  $C$ .

$$R_{ij} = \frac{D_i + D_j}{D_{ij}}; i, j = 1, \dots, C \quad (1)$$

$$r_i = \max(R_{ij}); \forall i \neq j; i, j = 1, \dots, C \quad (2)$$

$$R = \frac{1}{C} \sum_{i=1}^C r_i \quad (3)$$

$$\tau = \frac{\min(D_{ij})}{\max(D_k)}; i, j, k = 1, \dots, C \quad (4)$$

Here  $D_i$  and  $D_j$  are defined as the average distance between members within a cluster and  $D_{ij}$  as the distance between the respective cluster centers (see Fig. 1). The criterion  $R$  is then calculated from the maximum values of  $R_{ij}$  divided by the cluster numbers. The criterion  $\tau$  is calculated from the minimal distance  $\min(D_{ij})$  between members of clusters  $i$  and  $j$  and the maximum distance  $\max(D_k)$  of members within cluster  $k$ . Therefore  $R$  is a measure for the average compactness of all clusters and  $\tau$  is a measure

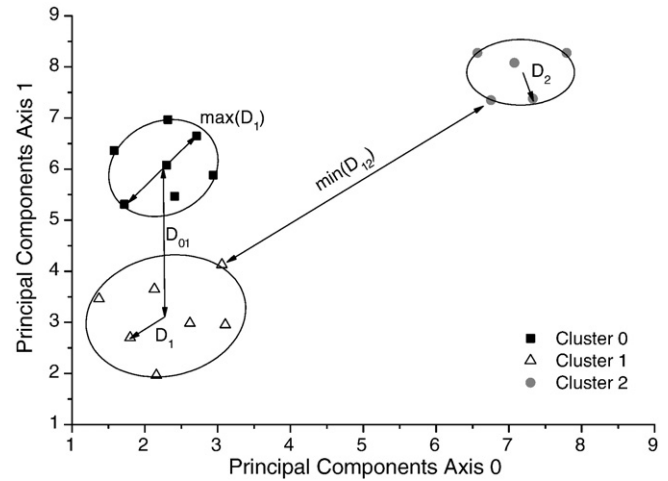


Fig. 1. Visualization of the definition of  $R$  and  $\tau$  criteria in principal components base.

for the mean spatial distribution of the clusters relative to each other. Hence the cluster members separate more distinctly for low values of  $R$  and high values of  $\tau$ . In order to find the number of AE-signal types with maximal separation an investigation of  $R$  and  $\tau$  as a function of cluster numbers is performed. The corresponding number of clusters for  $\min(R - \tau)$  usually reflects the number of waveform-types, that are distinguishable based on the applied pattern recognition technique. Such an approach has already been used to successfully identify distinct failure types in coated CFRPs and its results were validated using conventional AE-interpretations and advanced frequency distribution analysis combined with electron microscopy [17,18].

Apart from this qualitative correlation between AE features and associated failure mechanisms, we compare the recorded AE-energy contributions of each cluster to the micro-mechanical energy of the associated failure mechanism released during fracture.

### 2.2. Fracture energy approach

For stable crack propagation, proportionality between the waveforms acoustic emission energy release rate and the associated failures micro-mechanical energy release rate has been reported by several authors for various materials, like in CFRP [19], wood [20] and concrete [21].

Here, for a quantitative comparison with acoustic emission results, we calculate the micro-mechanical energy in a linear elastic fracture mechanics (LEFM) approach for crack propagation in opening mode (mode-I). As concluded from microscopic observations, three different types of failure are generated during mechanical loading of the coating. Mode-I crack growth occurs between nickel and copper layer, which will further be referred to as delamination. In addition, an independent mode-I crack growth in each coating layer (copper and nickel) was observed [17,18].

The direct proportionality between the acoustic emission energy release rate  $\partial E_{AE}/\partial t$  and the micro-mechanical energy release rate of the associated failure mechanism  $\partial E_{MM}/\partial t$  for stable crack growth can be written as:

$$\frac{\partial E_{MM}}{\partial t} = \alpha \frac{\partial E_{AE}}{\partial t} \quad (5)$$

This equation states, that a constant fraction of the energy released during crack growth is converted to an acoustic wave. The majority of the energy necessary for crack growth is consumed by plastic deformation, formation of new surfaces and dissipative processes. Acoustic emission constitutes only a small fraction of this energy. The relative size of these different energy contributions depends on the

shape of the crack tip and on the mechanical properties of the material. Different types of failure result in different direction dependencies of the intensity of sound radiation. The relative orientation between AE-source and detector can thus lead to different detected acoustic wave energies. Especially for thin plate specimens, the direction of sound radiation can result in different ratios of lamb wave modes, which in turn influence the overall energy content of the recorded signal [11] and therefore influence the proportionality constant  $\alpha$ .

Additionally, the energy content of the wave is reduced due to geometric spreading and velocity dispersion and depends on the path of propagation between AE-origin and point of detection. The sensor couplings transmissive properties and finally the recording equipment itself determine the electrical energy content of the signal [5]. Therefore  $\alpha$  should only be treated as a constant for one specific type of failure within one type of material and one experimental setup.

In our experiments a load dependent crack growth rate was observed. To obtain the accumulated AE-energy contribution and the associated accumulated micro-mechanical fracture energy, we integrate Eq. (5) over the time span of our experiment. In the following we assume, that our microscopic observations after mechanical loading reflect the damage progress at the final stage of our experiment. The acoustic emission energy  $E_{AE}$  of a single waveform is calculated from the amplitude  $s(t)$  of the recorded waveform with signal duration  $T$ . The amplitude is normalized by the input impedance  $W$  of the used measurement setup, i. e.:

$$E_{AE} = \int_0^T \frac{s^2(t)}{\Omega} dt \quad (6)$$

The fracture energy  $E_{MM}$  is derived from the stress-intensity concept of linear elastic fracture mechanics. From Irwin's modification of Griffith's energy relation, the strain energy release rate  $G$  is written as [22]:

$$G = - \left[ \frac{\partial E_{MM}}{\partial A} \right]_{z=\text{const.}} \quad (7)$$

Eq. (7) relates the energy  $E_{MM}$ , which is consumed to increase the free surface of a solid by the area  $A$ , to the value  $G$  at a given constant displacement  $z$ . Hence, we can rewrite Eq. (5) for each distinct failure mechanism:

$$\frac{\partial E_{MM}}{\partial t} = \frac{\partial A}{\partial t} G = \alpha \frac{\partial E_{AE}}{\partial t} \quad (8)$$

For known values of  $G$  (or correspondingly the stress-intensity factor  $K$ ) and the crack surface  $A$ , we can calculate their fracture energy and compare it to the recorded acoustic emission signals energy to yield the proportionality constant  $\alpha$ . We want to note, that the above approach assumes the applicability of linear elastic fracture mechanics. Since plastic deformation does not cause AE-signals the above approach is not applicable to cases where plastic deformation dominates. Hence, the LEFM approach will result in a conservative value for the fracture energy  $E_{MM}$ . To estimate the contribution of plastic deformation, the respective  $E_{MM}$  should be obtained from extended fracture mechanic approaches, like the J-integral concept, to yield valid  $\alpha$ -values.

### 3. Experimental

For experimental investigations eight rectangular CFRP-specimens according to DIN-EN-ISO 14125 (class IV type) were investigated in four-point bending (see Fig. 2). The specimen dimensions are  $(100 \pm 10) \text{ mm} \times (15 \pm 0.5) \text{ mm} \times (2 \pm 0.2) \text{ mm}$  ( $l \times w \times h$ ), the matrix consists of a polyurethane based epoxy resin (Araldite: LY 564/HY 2954).

Carbon fibers of type SIGRATEx KDK 8054/120 are arranged in six plies ( $0^\circ$ – $90^\circ$  textured) of woven fabric. The CFRP substrates were coated by chemical deposition of a 10  $\mu\text{m}$  Ni-layer to form a conductive surface and were subsequently electroplated with Cu-layers of 10  $\mu\text{m}$  and 30  $\mu\text{m}$  with dimensions of  $(25 \pm 1) \text{ mm} \times (15 \pm 0.5) \text{ mm}$  ( $l \times w$ ). We will refer to these different types of coatings as NiCu10 and NiCu30-specimens. Bending tests were performed according to DIN-EN-ISO 14125 with a distance between inner supports of  $(27 \pm 1) \text{ mm}$  and an outer distance of  $(81 \pm 2) \text{ mm}$ , respectively. An Instron type 8502 and a Zwick type 1464 were used for mechanical tests of the specimens. For all four-point bending tests the specimen was oriented with the coating on the tensile loading side (specimen bottom), which corresponds to the outer side of a pressurized vessel. In previous investigations it was demonstrated, that the CFRP substrate does not release acoustic emission below a strain value of  $\varepsilon = 0.8\%$  [17]. Hence, this value was chosen as strain limit in this investigation. During mechanical loading the acoustic emission was detected by two Physical Acoustics type WD wideband sensors in linear geometry. For acoustic coupling Baysilone silicone grease of medium viscosity was used, the mechanical contact was provided by two clamps. To decrease detection of friction noise a band pass ranging from 20 kHz up to 3 MHz was used. The AE waveforms were recorded using a PCI-2 data acquisition system with 40 dB preamplification and the software AEWIn (manufacturer: Physical Acoustic Ltd.) with a threshold of 40 dB and a sampling rate of 10 MS/s.

To determine the stress-intensity factor  $K_I$  for the two different copper layers, five center-notched specimens with  $(25 \pm 1) \text{ mm} \times (14 \pm 0.5) \text{ mm}$  ( $l \times w$ ) for each coating thickness of 10  $\mu\text{m}$  and 30  $\mu\text{m}$  were prepared. The initial crack length of  $(7.0 \pm 0.5) \text{ mm}$  was prepared using a scalpel and an adjacent precrack initiation realized by cyclic loading with 0.1 mm/min up to a gross-section stress of 30 MPa. Afterwards the precrack length was determined microscopically. The specimen was then loaded with constant velocity of 1 mm/min and the value for the critical load was determined from load-displacement curves. To obtain the size of the crack length we investigated the coating fracture in an environmental scanning electron microscope type XL30 (manufacturer: FEI Company).

A comparable determination of  $K_I$  for Ni-cracking was not possible, since the Ni-coating could not be lifted off the substrate, due to its dense initial crack network and strong adhesion to the substrate (see Section 5).

For coating delamination, the strain energy release rate  $G_I$  was determined from three peeling tests per coating thickness according to ASTM B533-85. Consequently the coating of the CFRP-specimens was carefully lifted off at one edge and pulled down to determine  $G_I$  from the peeling force. To measure the delaminated area between Ni and Cu layer a scanning acoustic microscope with 100 MHz transducer frequency and 1.5 mm focal length in pulse-echo mode was used (manufacturer: PVA Tepla).

### 4. Acoustic emission analysis

The acoustic emission signals recorded during bending experiments were first localized in linear geometry and only signal sources within a distance of 12.5 mm from the specimen center with the same extent as the coating were considered for further investigation. This step is used to exclude transient friction signals, that originate from the positions of the lower supports. The sound velocity used for localization was calculated from mutual sensor pulses travel times to be  $5500 \pm 500 \text{ m/s}$ . The uncertainty includes an error assumption for delay time determination and geometry, which results in a total error for AE-source localization of  $\pm 1.5 \text{ mm}$ . It is well known, that plate wave propagation occurs mainly within the CFRP and that the influence of the coating application is negligible. This is consistent with the observation, that the coating thickness has no influence on the measured sound velocity within the accuracy of the setup. The

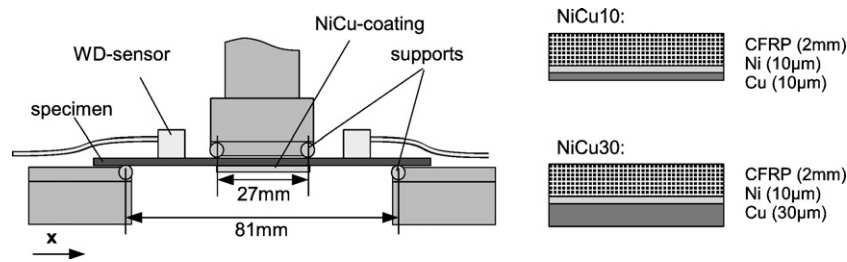


Fig. 2. Experimental setup (left) and cross-sectional drawing of NiCu coating composition (right).

signals localized were subjected to a “noise” reduction routine implemented within the software Noesis (manufacturer: Enviroacoustics S.E.).

This consists of a supervised classification algorithm to detect signals that could deteriorate clustering results:

- Manual definition of one dataset with “noise” signal types and one dataset with defined waveforms
- Selection of characteristic waveform parameters that allow highest discrimination between noise signals and defined waveforms
- Training of classification algorithm based on a back-propagating neural network to detect “noise” signal types in any dataset.

To provide higher discrimination efficiency and better algorithm performance, the features were normalized and projected to their principal components axis [23]. The “noise” signal types were excluded from the further investigation. Two characteristic types of signals excluded are shown in Fig. 3. These are signal types that exhibit more than one signal burst due to triggering errors, or “non-transient” signals arising from friction. Another source of signals unrelated to micro structural changes within the specimen is electromagnetically induced noise.

From the remaining waveforms, nine features were extracted within Noesis after the measurement to characterize the waveforms (see section 2.1). The features used are listed in Table 1 together with their definitions. Amplitude, absolute energy and average signal level were used, since a strong correlation to the underlying AE-source is expected. In addition, rise- and decay-angle were included to take into account the overall shape of the waveform. The shape should reflect,

at least to some extent, plate wave mode composition which in turn can reflect the underlying source mechanism [11]. Further, four frequency features are used to take into account frequency composition changes, which are due to different sound radiation directions that originate from different failure types.

After a principal components axis transformation the nine features were projected to the principal axis and normalized to a range from  $-1$  to  $1$  divided by their standard deviation [23]. Application of the  $R-\tau$  method results in either two or three distinguishable types of waveforms for all specimens investigated. The different types are marked by individual colors (red, green, blue) shown in the projection to the plane spanned by the 1st and 2nd principal components axis in Fig. 4. Accordingly either two (copper cracking and nickel cracking) or three (additional delamination) failure mechanisms were observed microscopically. This is described in more detail in [17] and [18]. Fig. 5 shows the result of the classification marked in different colors, projected onto the amplitude–energy plane.

Correlation between the clusters and associated failure mechanisms were established based on AE-source location, frequency of occurrence and frequency distribution. To calculate the average frequency spectrum of each cluster the software package AWARE++ was used [24]. In the frequency domain the difference of spectral weight between frequencies above and below 400 kHz can indicate a different direction of sound radiation [19]. This difference was used to distinguish delamination AE-signals from AE-signals belonging to cracks within the nickel or copper layer [17].

For each cluster, the AE-energy contributions of all corresponding waveforms were added over the loading time. For one representative

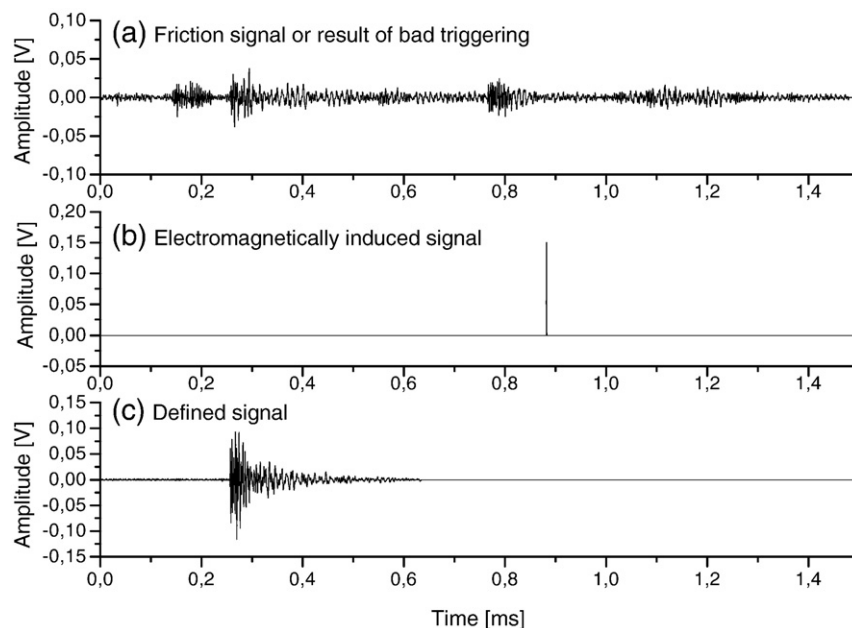


Fig. 3. Typical AE-signals recorded during measurement. Typical signal from friction or result of bad triggering (a), electromagnetically induced signal (b) and well triggered signal used for pattern recognition (c).



**Table 1**  
Extracted waveform features used for pattern recognition.

Feature	Definition
Amplitude	$A_{\max} = 20 \log(U_{\max}/1 \mu V) - dB_{\text{Preamplifier}}$ “maximum amplitude of waveform” [dB]
Absolute energy	$E_{\text{AE}} = \int_0^T U^2(t) dt$ “signal energy” [ $10^{-18}$ J]
Average signal level	$ASL = \sqrt{\frac{1}{T} \int_0^T A^2(t) dt}$ “root mean square of dB-amplitude $A(t)$ ” [dB]
Rise angle	$\phi_{\text{rise}} = \tan\left(\frac{A_{\max}}{t(A_{\max})}\right)$ “rising slope of signal” [rad]
Decay angle	$\phi_{\text{decay}} = \tan\left(\frac{A_{\max}}{T - t(A_{\max})}\right)$ “decay slope of signal” [rad]
Partial power 1–4	$\int_{f_1}^{f_2} \text{FFT}(U^2(t)) df / \int_0^{200 \text{ kHz}} \text{FFT}(U^2(t)) df$ “spectral weight contribution of given frequency range” [%] Partial power 1: $f_1 = 0$ kHz; $f_2 = 180$ kHz Partial power 2: $f_1 = 180$ kHz; $f_2 = 366$ kHz Partial power 3: $f_1 = 366$ kHz; $f_2 = 620$ kHz Partial power 4: $f_1 = 620$ kHz; $f_2 = 1200$ kHz

NiCu30-specimen the evolution of the accumulative AE-energy in time is shown in Fig. 6 for the three respective clusters. In the following, the accumulated AE-energy value achieved at the end of the experiment is compared to the micro-mechanical energies released during fracture as calculated from the LEFM approach.

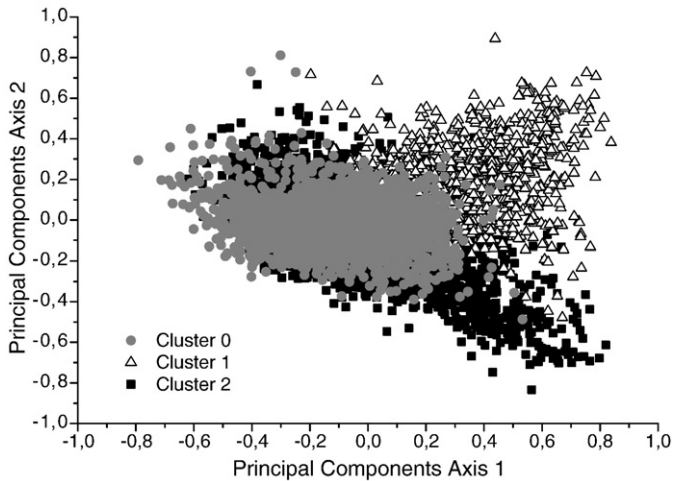


Fig. 4. Principal components axis projection for one representative NiCu30-specimen.

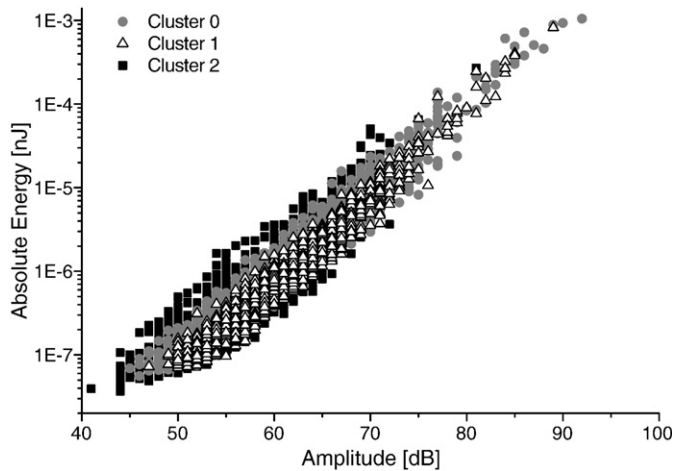


Fig. 5. Projection to amplitude–energy plane for one representative NiCu30-specimen.

**5. Fracture mechanics**

Although the clustering approach and microscopic observations yielded three distinct failure types, in the following we only investigate the relation between micro-mechanical energies and AE-energies for copper cracking and Ni–Cu delamination. A comparison between fracture energy for nickel crack growth and the associated AE-signals cluster will not be performed for the following reasons:

The nickel cracks appear below the copper layer, i. e. their crack length cannot be determined directly via electron microscopy in top-view. On purely nickel coated CFRP-specimens initial crack networks with varying density depending on the individual specimen were observed. This crack network grows only slightly during mechanical loading in comparison to the initial crack density. Therefore the crack progress can only be determined very inaccurately from top-view images or cross-sectional images, i. e. the standard deviation is unacceptably large. This small increase in the crack surface area is also reflected in the acoustic emission energies in Fig. 6, which are smaller for nickel than for copper crack growth. In comparison, the crack growth within the copper layer is much larger and will hence be discussed in the following.

**5.1. Fracture energy of copper cracking**

In contrast to the nickel layer, the copper layer is crack free. Under mechanical loading, a growing formation of single crack paths orthogonal to the loading axis ( $x$ -direction) with minor branching was observed. After unloading, the whole coating surface was investigated with scanning electron microscopy and the overall crack length  $l$  determined from images in top-view using ImageJ (see Fig. 7) [25]. Under the assumption that the crack propagation within the copper layer is a “crack-through” process (crack tip stops at Ni–Cu interface), the total crack surface area can be estimated as:

$$A = 2ld \tag{9}$$

The average thickness  $d$  of the two different copper layers were estimated from scanning electron microscopy cross-sectional images to be  $11.1 \pm 2.9 \mu\text{m}$  and  $32.3 \pm 3.7 \mu\text{m}$ , respectively. An image of a breaking edge originating from a tensile test on an according center-notched specimen is shown in Fig. 8.

To determine the stress-intensity factor for mode-I cracks  $K_I$ , copper coatings were lifted off their substrates and a centre-notched specimen as shown in Fig. 9 was prepared. In general, specimen geometries that permit plain strain conditions are used to obtain  $K_I$ . In our case, the given coating geometry applies rather to plane stress

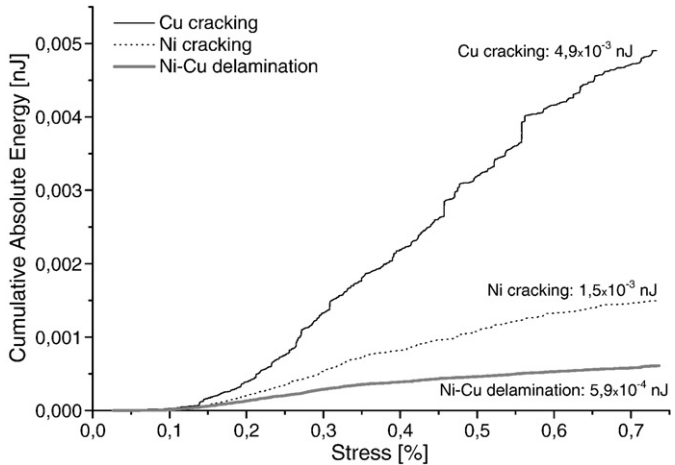


Fig. 6. Cumulative acoustic emission energy versus strain for the three failure types observed in NiCu30.

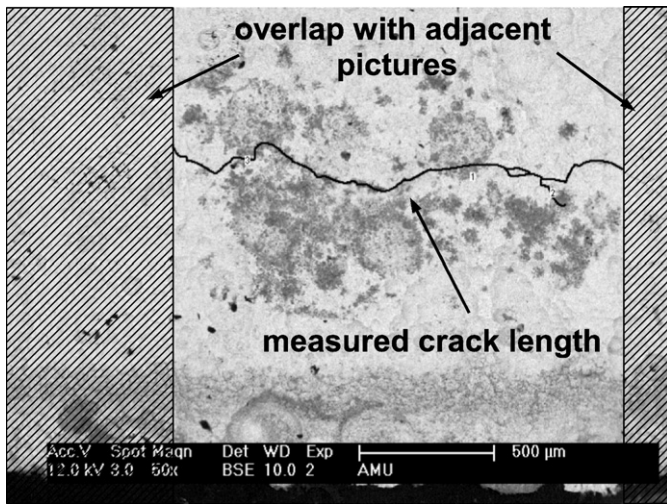


Fig. 7. Determination of copper crack length from scanning electron microscopy images.

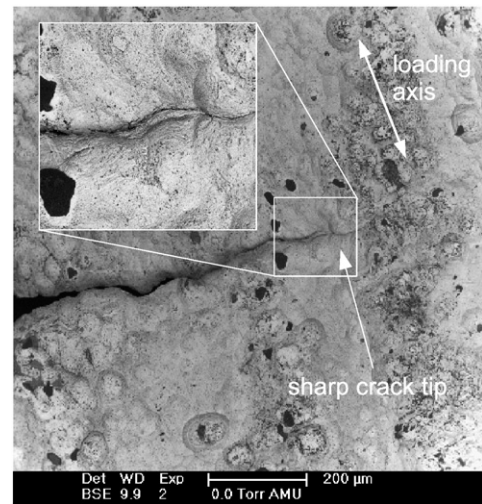


Fig. 10. Scanning electron microscopy pictures (top-view) of the crack tip in NiCu30 with sharp crack tip.

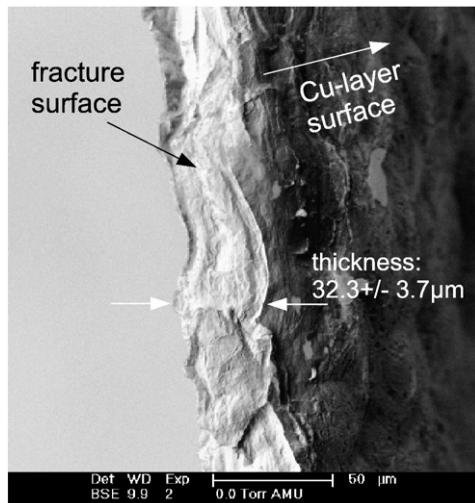


Fig. 8. Cross sectional image of 30 μm copper coating after fracture in tensile testing.

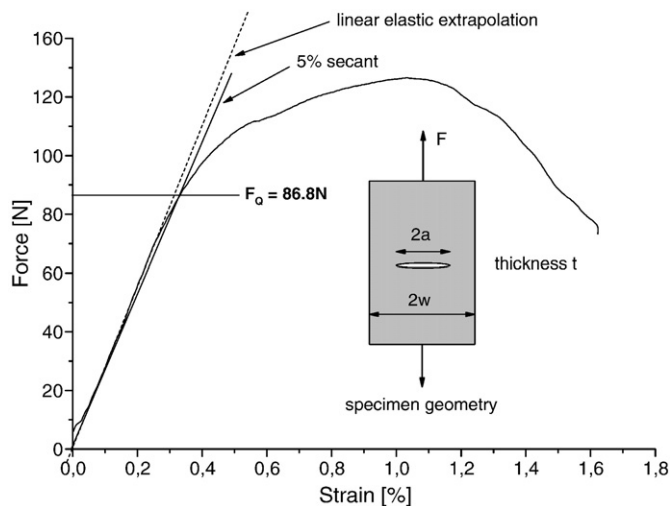


Fig. 9. Center-notched-tension specimen geometry and determination of stress-intensity factor  $K_I$  from force-strain curve. Dashed line marks linear elastic extrapolation, straight line marks 5% secant used for determination of  $F_0$ .

conditions, which was demonstrated using numerical simulations and measurements on Ni-based metal foils [26]. Therefore this was used for calculation of  $K_I$ . We further assumed a Young's modulus for the copper coatings of 130 GPa [27].

$$G_I = \frac{K_I^2}{E} \quad (10)$$

The critical load  $F_0$  is determined from the intersection of the load-displacement curve and the 5%-secant of the linear elastic range analogous to ASTM-E399, like shown in Fig. 9. The geometric dimensions of our specimens entering the calculation are foil-thickness  $t$ , width  $2w$  and precrack length  $2a$ .

$$K_I = 1.12 \frac{F_0}{2wt} \sqrt{\pi a} \cdot Y\left(\frac{a}{w}\right) \quad (11)$$

For our specimen dimensions the geometric correction function  $Y(a/w)$  is [28]:

$$Y\left(\frac{a}{w}\right) = \frac{1 - 0.5a/w + 0.326(a/w)^2}{\sqrt{1 - a/w}} \quad (12)$$

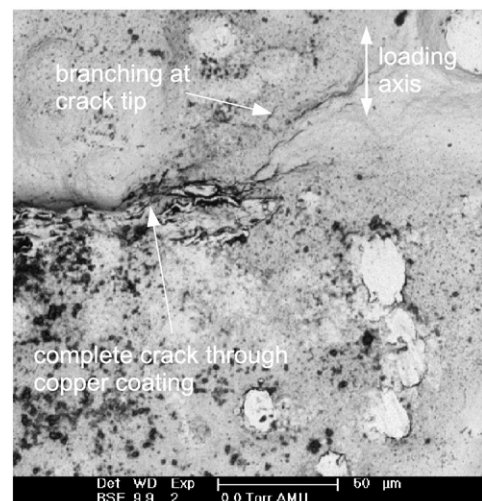


Fig. 11. Scanning electron microscopy pictures (top-view) of the crack tip in NiCu10 with crack branching.

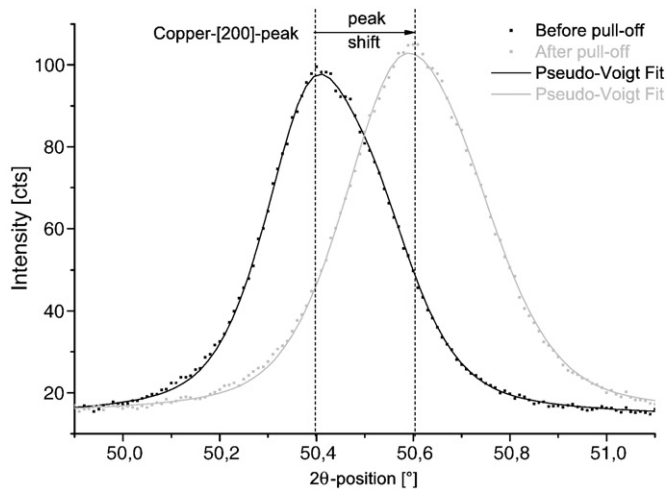


Fig. 12. X-Ray diffraction pattern of Cu-[200]-peak before and after coating pull-off.

Following the procedure described above, we calculated the strain energy release rate to be  $7460 \pm 2932 \text{ J/m}^2$  for  $10 \mu\text{m}$  Cu-coatings and  $5412 \pm 2376 \text{ J/m}^2$  for  $30 \mu\text{m}$  Cu-coatings, respectively. The values reported on copper coatings with similar thickness show scattering in their order of magnitude, depending on treatment and crystal structure [29,30].

While [29] and [30] report an increase in  $G_I$  with coating thickness in ranges below  $300 \mu\text{m}$ , we observed a decrease with increasing thickness in our investigation. In general, the thickness dependence of  $G_I$  is attributed to boundary effects, which can change the relative amount of energy dissipation at the crack tip. This is due to the fact, that the stress-fields are different in the boundary (surface) region compared to the bulk and that the surface microstructure can lead to an increased strain concentration at the crack tip, which reduces the macroscopic fracture toughness. With decreasing coating thickness boundary effects become more important. To explain the observed decrease in fracture toughness with increasing thickness in our case, the shape of the crack tips was analyzed using scanning electron microscopy.

Figs. 10 and 11 show SEM-images in top-view of crack patterns of the two different coatings. In the  $30 \mu\text{m}$  Cu-coatings the crack propagates orthogonal to the loading axis with a very sharp crack tip opening displacement. In contrast, in the  $10 \mu\text{m}$  Cu-coatings large branching is observed ahead of the crack tip and in addition, the crack orientation angle changes during tensile loading, since the crack

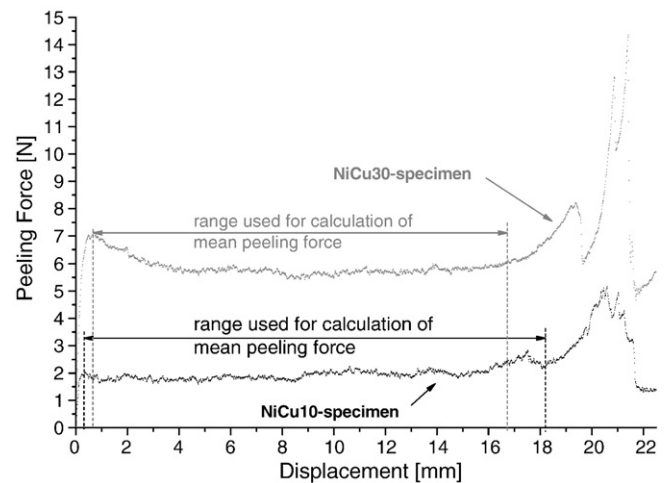


Fig. 14. Measurement of interfacial fracture toughness  $G_{III}$  for NiCu10 and NiCu30 specimens.

grows along flaws. Both effects increase the total amount of energy necessary for crack propagation and thus the fracture toughness.

The different crack appearance of the two coatings could be attributed to the growing influence of surface inhomogeneities for the thinner coating. In contrast, such surface inhomogeneities are expected to play only a minor role in metal foils as investigated by [30], compared to electroplated coatings on rough substrates.

Another reason for an increase of fracture toughness can be compressive stress present within the coating. Such stress should be reflected in the peak-shape and -position of X-Ray reflections. Eight coatings were analyzed by X-Ray diffraction applied on the CFRP and again after pull-off (see Fig. 12). The diffraction patterns of the respective coating type exhibit a peak shift before and after pull-off, characteristic for compressive macro-stress ( $151 \pm 19 \text{ MPa}$ ) which is the same in both coatings within the margin of error. We conclude that a pre-existent macro-strain is not responsible for the differences in fracture toughness observed.

## 5.2. Fracture energy of nickel–copper delamination

In four of the eight specimens in addition to crack growth within the nickel and copper layer delamination between the nickel and copper layer was observed. This appearance of a third failure mechanism is consistent with AE-pattern recognition, which indicates

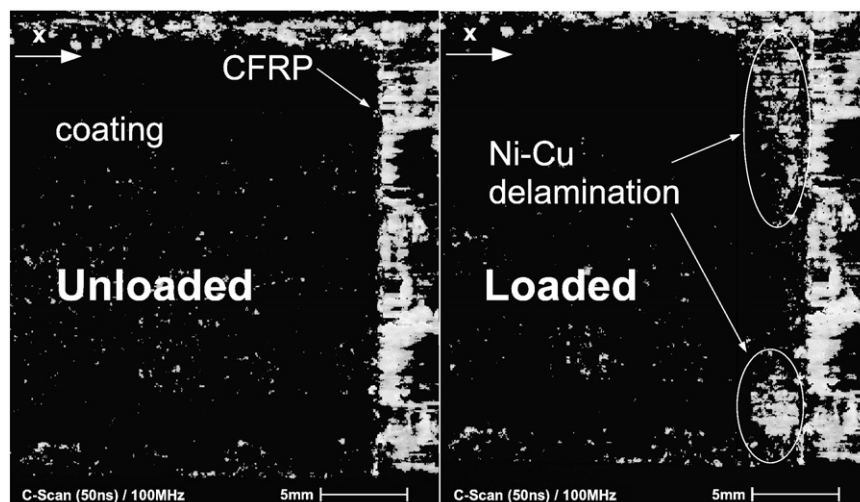


Fig. 13. Ultrasonic C-scan images of specimen NiCu30 before (left) and after mechanical loading (right).



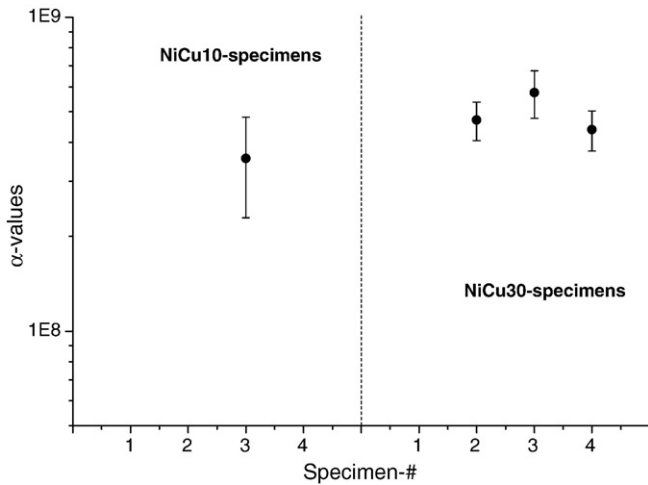


Fig. 15. Comparison of proportionality constants  $\alpha$  of the four specimens showing Ni-Cu delamination.

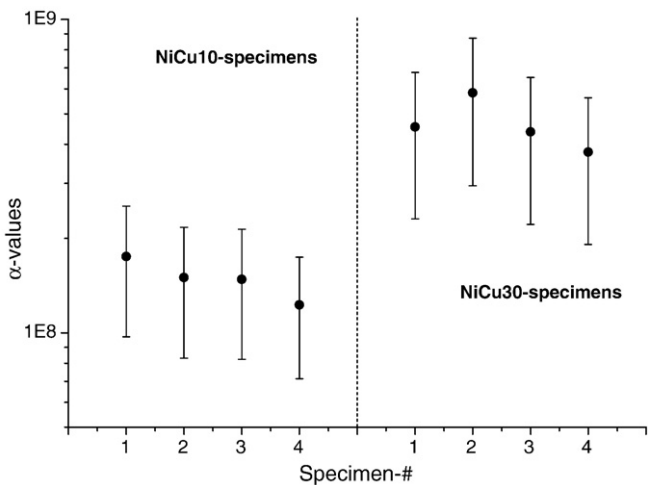


Fig. 16. Comparison of proportionality constants  $\alpha$  for Cu cracking of all specimens.

three instead of two separable types of acoustic emission signals. To quantify the delaminated area the specimens were investigated by scanning ultrasonic microscopy. Using a transducer with 100 MHz frequency and 1.5 mm focal length, all specimens were examined before and after mechanical loading (see Fig. 13).

In order to determine the area of delamination, depth-staggered C-scans with a total penetration depth of 50 ns were used, which correspond to a sound travelling path of 240  $\mu\text{m}$  in pure copper. This is much larger than the coatings approximate thickness of 30  $\mu\text{m}$  and

therefore reflection signals from the CFRP substrate are expected as well. For delaminated areas the reflexion coefficients change from 0.034% for a Cu–Ni interface to 100% for Ni–Air interfaces and almost 74%–93% for water–CFRP or water–Ni interfaces. These high intensity reflections can easily be detected within the ultrasonic C-scan images and their area was quantified using the software ImageJ. The delamination present after loading at the positions of high reflexions could also visually be verified. In order to quantify the delaminated area correctly, the roving textured CFRP-surface and according displacements in the relative depth were taken into account. An example for a quantification of a delaminated area (marked in white) is shown in Fig. 13. To obtain the strain energy release rate for delamination, peeling tests according to ASTM B533-85 were conducted, although the geometry of the specimens does not completely correspond to ASTM B533-85. As stated in [31], the influence of plastic deformation at the interfacial crack tip is negligible, if the interfacial tensile adhesion is much smaller than the yield strength of the coating material. Therefore, the calculated peeling strength is assumed to reflect the interfacial fracture toughness value  $G_{I/II}$ . The peeling test was conducted by pulling down the preliminary peeled edge and measurement of the necessary force. At the beginning of the peeling test, the load sharply increases until crack growth is initiated and reaches a constant peeling force during stable crack propagation. At the end of the measurement, the detected force increases drastically. This is most likely caused by inhomogeneities of the coating at its fringes. Therefore the average value between the onset of constant peeling force and the sharp peeling strength increase at the end was calculated, as indicated in Fig. 14. The values for  $G_{I/II}$  were calculated to be  $202 \pm 51 \text{ J/m}^2$  for 10  $\mu\text{m}$  coatings and  $385 \pm 15 \text{ J/m}^2$  for 30  $\mu\text{m}$  coatings.

## 6. Discussion and outlook

In Figs. 15, 16 and Table 2 the values for the proportionality constant  $\alpha$  according to Eq. (8) are shown for the specimens investigated. These values were calculated using  $G$  as determined from fracture toughness and peeling tests and the microscopically observed crack lengths and areas for copper cracking failure and delamination failure. In the case of delamination failure, the error in the determination of  $\alpha$  is large, since the quantification of the delaminated area is error-prone. In addition, the standard deviation of the  $G_{I/II}$ -value derived from peeling tests also contributes to the error in  $\alpha$ . In the case of copper cracking failure, large errors in  $\alpha$  originate from the size of standard deviations in the experimentally determined  $G_I$  values. These large standard deviations are attributed to inhomogeneous coatings on one hand, and the uncertainty in the range of linear elastic behaviour (see Fig. 9) on the other hand, which defines the critical load  $F_Q$  necessary for the calculation of  $G_I$ . In comparison, the inaccuracy of crack length determination via electron microscopy is negligible.

Table 2

Calculated values for  $\alpha$  derived from experimental values.

Failure-type	Specimen	AE-energy [J]	Crack area [ $\text{mm}^2$ ]	G-value [ $\text{J/m}^2$ ]	$\alpha$ -Value [ $10^{-8}$ ]
Cu cracking	NiCu10-1	$6.75 \times 10^{-12}$	$0.159 \pm 0.008$	$7460 \pm 2932$	$1.75 \pm 0.78$
	NiCu10-2	$5.15 \times 10^{-12}$	$0.104 \pm 0.005$	$7460 \pm 2932$	$1.50 \pm 0.67$
	NiCu10-3	$1.00 \times 10^{-11}$	$0.199 \pm 0.010$	$7460 \pm 2932$	$1.48 \pm 0.66$
	NiCu10-4	$2.68 \times 10^{-11}$	$0.442 \pm 0.011$	$7460 \pm 2932$	$1.23 \pm 0.52$
	NiCu30-1	$1.04 \times 10^{-11}$	$0.873 \pm 0.044$	$5412 \pm 2376$	$4.54 \pm 2.23$
	NiCu30-2	$3.73 \times 10^{-12}$	$0.402 \pm 0.020$	$5412 \pm 2376$	$5.83 \pm 2.88$
	NiCu30-3	$4.90 \times 10^{-12}$	$0.396 \pm 0.020$	$5412 \pm 2376$	$4.38 \pm 2.16$
	NiCu30-4	$6.84 \times 10^{-12}$	$0.477 \pm 0.024$	$5412 \pm 2376$	$3.77 \pm 1.86$
Ni–Cu delamination	NiCu10-3	$1.26 \times 10^{-10}$	$221.3 \pm 22.1$	$202 \pm 51$	$3.55 \pm 1.26$
	NiCu30-2	$8.76 \times 10^{-12}$	$10.7 \pm 1.1$	$385 \pm 15$	$4.71 \pm 0.66$
	NiCu30-3	$5.90 \times 10^{-13}$	$0.9 \pm 0.1$	$385 \pm 15$	$5.76 \pm 0.99$
	NiCu30-4	$2.49 \times 10^{-12}$	$2.8 \pm 0.3$	$385 \pm 15$	$4.38 \pm 0.64$



For delamination failure, the proportionality between calculated micro-mechanical energy and accumulated AE-energy is remarkably good for both coating thicknesses (see Fig. 15). This becomes especially clear, comparing the changes of AE-energy contributions to delamination between specimen NiCu30-2 and NiCu30-3. Here, a drop of more than one order of magnitude is observed. Accordingly the delaminated area measured via scanning acoustic microscopy decreases from 10.7 mm<sup>2</sup> to 0.9 mm<sup>2</sup>, resulting in a constant value for  $\alpha$  within the experimental error.

In contrast, the  $\alpha$ -values for copper cracking failure agree very well only within one coating thickness, but decrease by an approximate factor of three going from 30  $\mu$ m Cu-coating to 10  $\mu$ m Cu-coating thickness (see Fig. 16). This is consistent with Lysak et al., who reported, that in case of a crack-through process, the emitted AE-energy during fracture only depends on the crack length increment, but not on the newly created surface area [10]. Since the micro-mechanical fracture energy is proportional to the newly formed crack surface area, the proportionality constant between AE-energy and micro-mechanical energy changes as a function of coating thickness. This expected behaviour agrees well with the experimentally observed ratio between the mean  $\alpha$ -values of both coatings.

The current investigation shows that pattern recognition techniques applied to acoustic emission signals can successfully be used to identify different failure mechanisms within coatings. Beyond merely correlating acoustic emission signals and failure mechanisms, it is shown, that the failure specific AE-energies are a measure of the corresponding fracture energies derived from LEFM approaches. This offers the general possibility to adapt the method for comparative failure investigations on coated materials. It should be noted that these kinds of measurements are expected to yield even better results in case of coated metals, since the acoustic emission from the substrate is less in this case.

## Acknowledgments

We thank Dr. D. Schultheiß from BMW Group research and Technology for providing the specimens used in this investigation.

## References

- [1] D. Schultheiß, Permeation Barrier for Lightweight Liquid Hydrogen Tanks, PhD-Thesis, University of Augsburg, 2007.
- [2] StorHy - Hydrogen Storage Systems for Automotive Application, Third Periodic Activity Report, 2007.
- [3] R. Beydon, G. Bernhart, Y. Segui, *Surf. Coat. Tech.* 126 (2000) 39.
- [4] J. Bohse, G.W. Mair, P. Novak, *Adv. Mater. Res.* 13–14 (2006) 267.
- [5] J. Bohse, *J. Acoustic Emission* 22 (2004) 208.
- [6] L. Fu, K. Khor, H. Ng, T. Teo, *Surf. Coat. Technol.* 130 (2000) 233.
- [7] X.Q. Ma, H. Cho, M. Takemoto, *Surf. Coat. Technol.* 139 (2001) 55.
- [8] J. Miguel, J. Guilemany, B. Mellor, Y. Xu, *Mat. Sci. Eng. A-Struct.* 352 (2003) 55.
- [9] E. Harry, M. Ignat, A. Rouzaud, P. Juliet, *Surf. Coat. Technol.* 111 (1999) 177.
- [10] M.V. Lysak, *Eng. Fract. Mech.* 55 (3) (1996) 443.
- [11] M.A. Hamstad, A.O. Gallagher, J. Gary, *J. Acoust. Emiss.* 20 (2002) 39.
- [12] W.H. Prosser, *J. Acous. Emiss.* 14 (1996) 1.
- [13] A.A. Anastassopoulos, T.P. Philippidis, *J. Acoust. Emiss.* 13 (1995) 11.
- [14] T.P. Philippidis, V. Nikolaidis, A.A. Anastassopoulos, *NDT E Int.* 31 (1998) 329.
- [15] D.L. Davies, D.W. Bouldin, *IEEE Trans. Pattern Anal.* 1 (1979) 224.
- [16] S. Bow, *Pattern Recognition-Application to Large Data-Set Problems*, first ed. Marcel Dekker Inc., New York, 1984.
- [17] M.G.R. Sause, D. Schultheiß, S. Horn, *J. Acous. Emiss.* 26 (2008) 1.
- [18] M.G.R. Sause, S. Horn, in: W. Krenkel (Ed.), *Verbundwerkstoffe*, Wiley-VCH, Weinheim, 2009, p. 474.
- [19] J. Bohse, J. Chen, A. Brunner, in: J.G. Williams, A. Pavan (Eds.), *Fracture of Polymers and Composites and Adhesives*, Elsevier, Amsterdam, 2000, p. 15.
- [20] E.N. Landis, D.B. Whittaker, *Acoustic Emission as a Measure of Fracture Energy*, Fourteenth Engineering Mechanics Conference, ASCE, May 21–24, Austin, Texas, 2000.
- [21] E.N. Landis, L. Baillon, *J. Eng. Mech-ASCE* 128 (6) (2002) 698.
- [22] N.E. Dowling, *Mechanical Behaviour of Materials*, second ed. Prentice Hall Inc., New Jersey, 1999.
- [23] Enviroacoustics S.E., NOESIS Advanced Acoustic Emission Data Analysis and Pattern Recognition & Neural Networks Software For Acoustic Emission Applications, 2006.
- [24] M.G.R. Sause, AWARE++ Software manual Rev. 1.0, <http://www.physik.uni-augsburg.de/exp2/downloads.de.shtml>, 2009.
- [25] U.S. National Institute of Health, ImageJ – Image Analysis and Processing in Java, 2009 <http://rsbweb.nih.gov/ij/index.html>.
- [26] L. Liu, J.W. Holmes, *J. Eng. Mater. Technol. ASME* 129 (2007) 594.
- [27] A.M. James, M.P. Lord, *Macmillan's Chemical and Physical Data*, twenty-fifth ed. Macmillan, New York, 1992.
- [28] H.P. Tada, C. Paris, G.R. Irwin, *The Stress Analysis of Cracks Handbook*, third ed. Professional Engineering Publishing, London, 2000.
- [29] A. Hadrboletz, B. Weiss, G. Khatibi, *Int. J. Fract.* 107 (2001) 307.
- [30] H.W. Wang, Y.L. Kang, Z.F. Zhang, Q.H. Qin, *Int. J. Fract.* 123 (2003) 177.
- [31] Y. Wei, J.W. Hutchinson, *Int. J. Fract.* 93 (1998) 315.